Three-dimensionally ordered mesoporous iron oxide-supported single-atom platinum: Highly active catalysts for benzene combustion

Kuan Yang, Yuxi Liu*, Jiguang Deng, Xingtian Zhao, Jun Yang, Zhuo Han, Zhiquan Hou, Hongxing Dai*

Beijing Key Laboratory for Green Catalysis and Separation, Key Laboratory of Beijing on Regional Air Pollution Control, Key Laboratory of Advanced Functional Materials, Education Ministry of China, Laboratory of Catalysis Chemistry and Nanoscience, Department of Chemistry and Chemical Engineering, College of Environmental and Energy Engineering, Beijing University of Technology, Beijing 100124, China

ABSTRACT

Single-atom catalysts are a kind of promising catalytic materials that can use the precious metal more efficiently. The KIT-6-templaing method was adopted to obtain three-dimensionally ordered mesoporous iron oxide (meso-Fe_2O_3). The meso-Fe_2O_3-supported single-atom Pt with a loading of x wt% (xPt_1/meso-Fe_2O_3, x = 0.08, 0.15, and 0.25) catalysts were synthesized via a polyvinyl alcohol-protected reduction route. The 0.25 Pt_1/meso-Fe_2O_3 sample showed much better catalytic activity than the meso-Fe_2O_3-supported Pt nanoparticle (0.25 Pt_{NP}/meso-Fe_2O_3) sample for benzene combustion, with the temperatures $T_{10\%}$, $T_{50\%}$, and $T_{90\%}$ (corresponding to benzene conversions of 10, 50, and 90%) were 164, 186, and 198 °C at a space velocity of 20,000 mL/(g h), respectively. The TOF_{Pt} (2.69 s^{-1}) obtained over 0.25 Pt_1/meso-Fe_2O_3 at 160 °C was much higher than that (1.16 s^{-1}) obtained over the 0.25 Pt_{NP}/meso-Fe_2O_3 sample at 160 °C. Furthermore, the 0.25 Pt_1/meso-Fe_2O_3 and 0.15Pt_1/meso-Fe_2O_3 samples exhibited better water-resistant ability than the 0.25 Pt_{NP}/meso-Fe_2O_3 sample, which was possibly due to formation of the active radicals and decomposition of carbonates in the presence of moisture. In situ DRIFTS results demonstrate that the phenolate and benzoquinone as well as cyclohexanone and maleate were the main intermediates in the oxidation of benzene. The good stability of the 0.15Pt_1/meso-Fe_2O_3 and 0.25 Pt_1/meso-Fe_2O_3 samples was associated with the strong interaction between Pt and meso-Fe_2O_3.

1. Introduction

Most of volatile organic compounds (VOCs) are pollutants that are detrimental to the environment and humans [1], it is hence an urgent task to eliminate the VOCs. Numerous techniques, such as absorption, adsorption, incineration, and photocatalytic and catalytic combustion, are feasible to remove the VOCs [2–6]. Catalytic combustion is considered to be one of the most effective and economic methods for the oxidative removal of VOCs because of its high efficiency and low operation temperatures [2–4], in which the availability of high-performance catalysts is the key issue.

It is well known that the size of metal particles is a critical factor in determining the catalytic activity [7]. A catalytic reaction usually occurs on the surface of metals, in which only the surface atoms of the metal nanoparticles (NPs) participate in the reaction. Such a feature suggests that a large fraction of metal atoms cannot be utilized, leading to a low catalytic efficiency. Supported noble metal NPs play a paramount role in catalyzing the removal of VOCs in environmental

remediation [8,9]. Unfortunately, noble metals are expensive, which limits its wide applications. Consequently, considerable efforts have been devoted to optimize the use of noble metals by reducing their sizes to several nanometers or even dispersing them in single atom. For example, an iron oxide-supported Pt single-atom catalyst was first developed, and used in the "single-atom catalysis" [10]. This novel concept has sparked great interests in heterogeneous catalysis [11,12]. In the past few years, there have been a number of works focused on the single-atom catalysis. Noble metal (e.g., Au, Pd or Pt)-based single-atom catalysts were prepared using the different methods [13–15], and some applications in methanol steam reforming [16], water-gas shift reaction [17], oxygen reduction reaction [18], photocatalysis [19,20], and ethanol dehydrogenation [21] can be seen in the literature. In addition, non-noble metal single-atom catalysts were also used for various applications [18,21]. However, there have been so far no reports on the utilization of single-atom for the combustion of VOCs.

Previously, we prepared mesoporous transition metal oxides and their supported noble metal nanocatalysts (such as meso-Co_3O_4 [22],

* Corresponding authors.
E-mail addresses: yxliu@bjut.edu.cn (Y. Liu), hxdai@bjut.edu.cn (H. Dai).

Au/meso-Cr$_2$O$_3$ [23], and PdPt/meso-Mn$_2$O$_3$ [24]) using the KIT-6-templating and/or polyvinyl alcohol (PVA)-protected reduction strategies. It was found that these mesoporous materials showed good catalytic performance in the combustion of typical VOCs. In the present work, we report the preparation, characterization, and catalytic properties as well as water- and carbon dioxide-resistant behaviors of single-atom Pt supported on meso-Fe$_2$O$_3$ for benzene combustion.

2. Experimental

2.1. Catalyst preparation

Highly ordered mesoporous KIT-6 template was synthesized according to the procedures described in the literature [25]. The KIT-6 was synthesized in a mixed aqueous solution of *n*-butanol and HCl using the Pluronic P123 (MW = 5800 g/mol) as structure-directing agent and tetraethoxysilane (TEOS) as silica source. Briefly, 6 g of Pluronic P123 was dissolved in 217 mL of deionized water and 9.83 mL of HCl aqueous solution (37 wt%) at 50 °C. Under vigorous stirring for 40 min, 7.41 mL of *n*-butanol was added. After stirring for 1 h, 13.8 mL of TEOS was slowly added to the above homogeneous solution. The mixture was stirred at 35 °C for 24 h, followed by hydrothermal treatment at 100 °C for 24 h. The obtained solid product was filtered, washed several times with deionized water and alcohol, and then dried at 60 °C for 12 h, and finally calcined in air at 550 °C for 4 h, thus obtaining the three-dimensionally (3D) ordered mesoporous KIT-6 template. 3D ordered mesoporous Fe$_2$O$_3$ was fabricated using 3D ordered mesoporous KIT-6 as hard template. Typically, 1.0 g of KIT-6 was added to 50 mL of toluene, and the suspension was stirred at 65 °C for 30 min and sonicated for 30 min. After that, 2.0 g of Fe(NO$_3$)$_3$·9H$_2$O was added to the mixture under vigorous stirring, followed by stirring at 65 °C for 5 h. Then, the suspension was filtered to get a precursor@KIT-6 composite that was dried in air at room temperature (RT) overnight. The dried precursor@KIT-6 composite was finally calcined in a muffle furnace. The temperature was from RT to 600 °C at the heating rate of 1 °C/min and kept at 600 °C for 2 h. Finally, the template-free meso-Fe$_2$O$_3$ was obtained after removal of the silica with a hot NaOH aqueous solution (2.00 mol/L), followed by centrifugation, washing with deionized water and ethanol, and drying at 80 °C. The obtained material was denoted as meso-Fe$_2$O$_3$.

The *x* wt% Pt$_1$/meso-Fe$_2$O$_3$ catalysts were prepared via a PVA-protected reduction route with PVA (MW = 10 000 g/mol) as protecting agent and NaBH$_4$ as reducing agent. The typical preparation procedures are as follows: A desired amount of Pt(NH$_3$)$_4$(NO$_3$)$_2$ aqueous solution (0.0010 mol/L) was added to the PVA (noble metal/PVA mass ratio = 1.0 : 1.2) in an ice bath under stirring, a moderate amount of meso-Fe$_2$O$_3$ dispersed in methanol was then added to the mixed solution (the theoretical Pt loadings (*x*) were 0.1, 0.2, and 0.3 wt%, respectively). The mixture was further vigorously stirred for 3 h. 0.05 g of NaBH$_4$ dissolved in deionized water was dropwise added to the mixed solution containing meso-Fe$_2$O$_3$, PVA, and Pt ions for the reduction of Pt ions and stirred for 1 h. After being filtered and dried at 60 °C in an oven, the solid was finally calcined at a ramp of 1 °C/min from RT to 550 °C and kept at this temperature for 2 h in a muffle furnace, hence obtaining the *x* wt% Pt$_1$/meso-Fe$_2$O$_3$ (denoted as *x*Pt$_1$/meso-Fe$_2$O$_3$) catalysts.

For comparison purposes, the meso-Fe$_2$O$_3$-supported Pt nanoparticles (0.25 wt% Pt$_{NP}$/meso-Fe$_2$O$_3$, denoted as 0.25 Pt$_{NP}$/meso-Fe$_2$O$_3$) catalyst was prepared via a PVA-protected reduction route and after calcination at 550 °C for 2 h in a muffle furnace. The detailed preparation procedure can be found in the Supplementary material.

All of the chemicals (A.R. in purity) were purchased from Beijing Chemical Reagent Company and used without further purification.

2.2. Catalyst characterization

All of the samples were characterized by means of techniques, such as inductively coupled plasma-atomic emission spectroscopy (ICP-AES), X-ray diffraction (XRD), transmission electron microscopy (TEM), high angle annular dark field (HAADF) and elemental mapping, in situ diffuse reflectance Fourier transform infrared spectroscopy (in situ DRIFT), nitrogen adsorption-desorption (BET), X-ray photoelectron spectroscopy (XPS), hydrogen temperature-programmed reduction (H$_2$-TPR), and CO chemisorption. The detailed characterization procedures are described in the Supplementary material.

2.3. Catalytic activity evaluation

A continuous flow fixed-bed quartz microreactor (i.d. = 6 mm) was employed for the measurement of catalytic activities at atmospheric pressure. Before the test, each sample was treated in an oxygen flow of 20 mL/min at 250 °C for 60 min. To minimize the effect of hot spots, the catalyst (50 mg, 40–60 mesh) was diluted with 0.25 g of quartz sands (40–60 mesh). The reactant mixture was composed of 1000 ppm benzene + 20.0 vol% O$_2$ + N$_2$ (balance). The 1000-ppm benzene was generated by passing a N$_2$ flow through a pure benzene-containing bottle that was chilled in an isothermal bath at 8 °C. The total flow rate was 16.6 mL/min, thus giving a space velocity (SV) of 20,000 mL/(g h). In the case of water vapor introduction, 1.0 and 3.0 vol% H$_2$O was introduced by passing the feed stream through a water saturator at 16 and 34 °C, respectively. In the case of CO$_2$ addition, 2.5 vol% CO$_2$ was introduced from a CO$_2$ cylinder with N$_2$ as balance gas. Reactants and products were analyzed online by gas chromatography (GC-14C, Shimadzu) with a flame ionization detector (FID), using a stabilwax-DA column (30 m in length) and a Carboxen 1000 column (3 m in length). Carbon balance was 99 ± 1.5% in each test. The benzene conversion is defined as ($c_{inlet} - c_{outlet}$)/c_{inlet} × 100%, where the c_{inlet} and c_{outlet} are the inlet and outlet benzene concentrations in the feed stream, respectively. The reaction rates and turnover frequencies (TOFs) were calculated at benzene conversions below 10%. The heat transfer effects could be avoided at low benzene conversions and low benzene concentrations in benzene combustion. Moreover, in the case of a reactor/particle diameter ratio higher than 10 and a catalyst bed length/particle diameter ratio higher than 50, the axial diffusion effect could be neglected [26].

3. Results

3.1. Crystal phase composition, morphology, and textural property

According to the ICP-AES characterization results, the obtained catalysts were composed of 0.08Pt$_1$/meso-Fe$_2$O$_3$, 0.15Pt$_1$/meso-Fe$_2$O$_3$, 0.25 Pt$_1$/meso-Fe$_2$O$_3$, and 0.25 Pt$_{NP}$/meso-Fe$_2$O$_3$ (Table 1), respectively. The diffraction peak at 2θ = ca. 1° in the small-angle XRD pattern (Fig. 1A) of meso-Fe$_2$O$_3$ and 0.25 Pt$_1$/meso-Fe$_2$O$_3$ indicates formation of a 3D ordered mesoporous structure with a cubic *Ia3d* symmetry. The loading of the precious metals did not induce a significant change in pore structure of meso-Fe$_2$O$_3$ (Fig. 1A). The wide-angle XRD patterns of meso-Fe$_2$O$_3$ and its supported Pt samples showed well-resolved reflections that could be indexed to the rhombohedral Fe$_2$O$_3$ phase (JCPDS PDF# 33-0664), and their typical crystal faces were indicated in the 0.25 Pt$_{NP}$/meso-Fe$_2$O$_3$ sample (Fig. 1B). No crystal phase of Pt was detected owing to good dispersion and the low metal loadings. The average crystallite sizes (D_c) calculated according to the Scherrer equation were 20–22 nm (Table 1).

Fig. 2 shows the TEM images of the meso-Fe$_2$O$_3$ and 0.25 Pt$_1$/meso-Fe$_2$O$_3$ samples. A high-quality mesoporous architecture was observed in each of the porous samples, in good consistency with the small-angle XRD results. It should be noted that TEM images (Fig. 2a–c) of the meso-Fe$_2$O$_3$ sample were recorded at different magnifications. As

Table 1
Crystal phase compositions, average Fe_2O_3 crystallite sizes (D_c), BET surface areas, pore diameters, pore volumes, and actual Pt loadings of the as-prepared samples.

Sample	Crystal phase	D_c[a] (nm)	Surface area (m^2/g)	Pore diameter (nm)	Pore volume (cm^3/g)	Actual metal content[b] (wt%)
meso-Fe_2O_3	Rhombohedral	20.0	90.5	5.6	0.23	–
0.08Pt$_1$/meso-Fe_2O_3	Rhombohedral	22.0	90.9	5.6	0.25	0.08
0.15Pt$_1$/meso-Fe_2O_3	Rhombohedral	21.1	91.9	5.6	0.22	0.15
0.25 Pt$_1$/meso-Fe_2O_3	Rhombohedral	20.6	89.8	5.6	0.21	0.25
0.25 Pt$_{NP}$/meso-Fe_2O_3	Rhombohedral	20.9	98.5	5.6	0.22	0.25

[a] Data were calculated according to the Scherrer equation using the FWHM of the (104) line of Fe_2O_3.
[b] Data were determined by the ICP-AES technique.

shown in the high-resolution TEM images of meso-Fe_2O_3 and 0.25 Pt$_1$/meso-Fe_2O_3, the intraplanar spacings (*d* values) were measured to be ca. 0.27 nm (Fig. 2c and f), in good consistency with those of the (104) crystal plane of the standard Fe_2O_3 (JCPDS PDF# 33-0664) sample. The observation of multiple bright electron diffraction rings in the SAED patterns (insets of Fig. 2b and d) of the meso-Fe_2O_3 and 0.25 Pt$_1$/meso-Fe_2O_3 samples suggests the formation of a polycrystalline structure. No Pt nanoparticles (NPs) were recorded in TEM image of the 0.25 Pt$_1$/meso-Fe_2O_3 sample (Fig. 2d–f). It is unambiguous that Pt was uniformly dispersed on the surface of 0.15 Pt$_1$/meso-Fe_2O_3 (Fig. 3A–D). The elemental mappings of the 0.25 Pt$_1$/meso-Fe_2O_3 sample reveal that Pt was uniformly dispersed on the surface of meso-Fe_2O_3 too (Fig. 3E–F). Indeed, aberration-corrected HAADF-STEM technique clearly demonstrates the existence of isolated Pt atoms with a high dispersion on the surface of 0.25 Pt$_1$/meso-Fe_2O_3 (Fig. 4), as can be seen from the additional aberration-corrected HAADF-STEM images with different regions of the 0.25 Pt$_1$/meso-Fe_2O_3 samples (Fig. S1). Pt NPs, however, can be clearly observed on the surface of the 0.25 Pt$_{NP}$/meso-Fe_2O_3 sample (Fig. S2).

In situ DRIFTS is a convincing characterization technique that can be applied to discriminate and quantify the concentration of platinum group metal isolated (PGM$_{iso}$) species in a catalyst, and provide insights into the local geometry, stability, reactivity, and homogeneity of the supported PGM$_{iso}$ species [27]. Since CO possessed several advantages in the characterization of the supported PGM$_{iso}$ species [28], CO adsorption behaviors of the samples were examined using the in situ DRIFTS technique, and their results are shown in Fig. 5. For the 0.25 Pt$_1$/meso-Fe_2O_3 sample, there was a quasi-symmetrical band at around 2073 cm^{-1} that could be rationally ascribed to the linearly adsorbed CO on the surface of Pt [29,30], substantiating the HAADF-STEM observation that Pt species were predominantly isolated on the

surface of 0.25 Pt$_1$/meso-Fe_2O_3. In the 0.25 Pt$_{NP}$/meso-Fe_2O_3 sample, however, Pt existed in the form of NPs on the surface of meso-Fe_2O_3, and CO at a stretching frequency of ca. 2060 cm^{-1} could be rigorously assigned to the linearly bounded to the Pt^0 sites [31]. CO adsorption on the Pt$_{metal}$ sites has been extensively studied. It is known that the stretching frequency of the linearly adsorbed CO is in the range of 2030–2100 cm^{-1}, which depends upon the coordination number of the Pt adsorption site and charge transfer between Pt$_{metal}$ and the support. Due to the coordination with O atoms on the surface of metal oxide supports or in the lattice of zeolites, the Pt$_{iso}$ species are expected to exist in a cationic charge state, which is manifested spectroscopically in a blueshifted (higher wavenumber) band position of CO adsorbed to the Pt$_{iso}$ as compared with the Pt$_{metal}$ sites (either in the linear or bridge adsorption geometry), in which the reported stretching frequencies were in the range of 2080–2170 cm^{-1} [28,32]. It has been reported that the stretching frequency of the CO on the Pt$_{iso}$ was shifted to higher frequencies as compared with that of the CO adsorbed in a linear geometry on the Pt$_{metal}$ clusters on the same support. Therefore, the exact stretching frequencies of CO adsorption on Pt$_1$/meso-Fe_2O_3 and Pt$_{NP}$/meso-Fe_2O_3 were highly dependent upon the direction and magnitude of charge transfer between the Pt and the support as well as the coordination number of the Pt adsorption site [27]. By combining the results from more aberration-corrected HAADF-STEM images of different regions (Fig. S1, in which we could find many Pt single atoms and no Pt NPs in 0.25 Pt$_1$/meso-Fe_2O_3) and the CO-DRIFTS results, we conclude that a single-atom Pt$_1$/meso-Fe_2O_3 catalyst was successfully synthesized.

Each sample displayed a type IV nitrogen adsorption–desorption isotherm with a clear H1 hysteresis loop at a relative pressure (p/p_0) of 0.4–0.9 (Fig. S3(A)), suggesting the presence of uniform mesopores. This result was in good agreement with those of the small-angle XRD
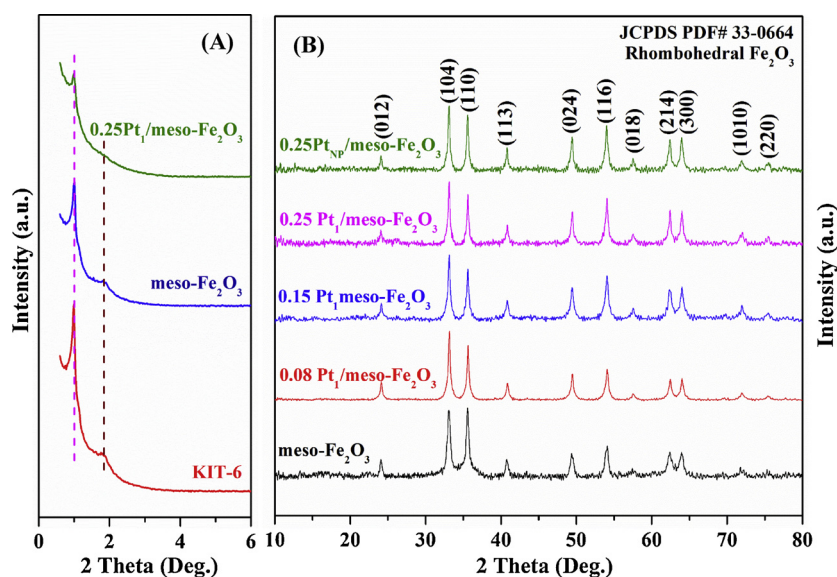

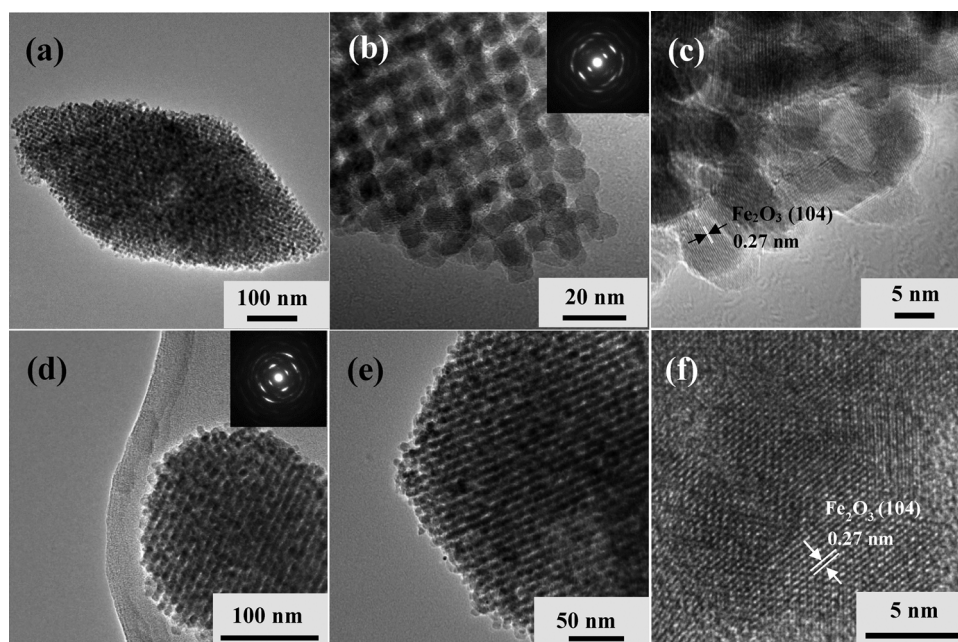**Fig. 1.** (A) Small-angle and (B) wide-angle XRD patterns of the as-prepared samples.

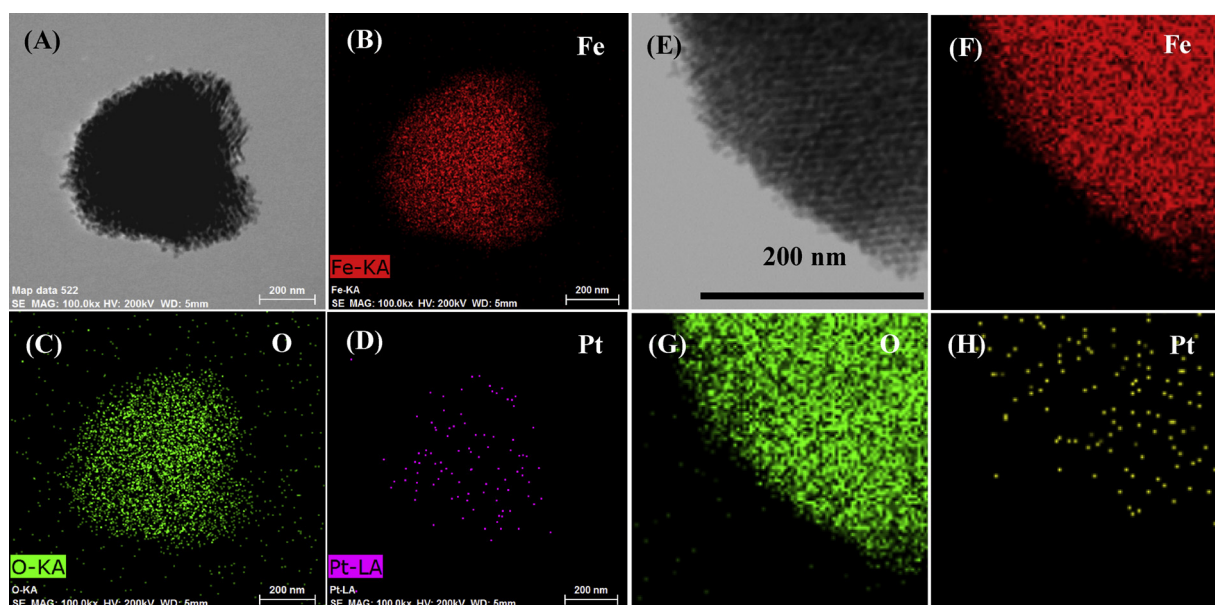**Fig. 2.** TEM images of (a–c) meso-Fe_2O_3 and (d–f) 0.25 Pt_1/meso-Fe_2O_3.

Fig. 3. Elemental mappings of (A–D) 0.15Pt_1/meso-Fe_2O_3 and (E–H) 0.25 Pt_1/meso-Fe_2O_3.

and TEM investigations. As shown in Fig. S3(B), the average pore sizes of the samples were 5.6 nm. Table 1 summarizes the textural parameters of the samples. The BET surface areas of the meso-Fe_2O_3, 0.08Pt_1/meso-Fe_2O_3, 0.15Pt_1/meso-Fe_2O_3, 0.25 Pt_1/meso-Fe_2O_3, and 0.25 Pt_{NP}/meso-Fe_2O_3 samples were 90.5, 90.9, 91.9, 89.8, and 98.5 m^2/g, respectively.

3.2. Surface element composition, metal oxidation state, and adsorbed oxygen species

XPS is an effective technique to investigate the surface element compositions, metal oxidation states, and adsorbed oxygen species of a sample. Fig. 6 shows the Fe 2p$_{3/2}$, O 1 s, and Pt 4f XPS spectra of the samples. As shown in Fig. 6A, the asymmetrical Fe 2p$_{3/2}$ signal could be decomposed into three components at binding energy (BE) = 710.5, 712.5, and 717.8 eV, assignable to the surface Fe^{2+} and Fe^{3+} species

and the satellite of the surface Fe^{2+} species [33], respectively. Fe^{2+} was generated by the reduction of $NaBH_4$ during the preparation of the xPt_1/meso-Fe_2O_3 catalysts, and the meso-Fe_2O_3 was also pretreated with $NaBH_4$ before catalytic test to maintain the consistency. It can be observed from Fig. 6B that the asymmetrical O 1 s spectrum of each sample could be deconvoluted into three components at BE = 529.7, 531.3, and 533.1 eV, attributable to the surface lattice oxygen (O_{latt}), adsorbed oxygen (O_{ads}, e.g., O_2^-, O_2^{2-} or O^-), and adsorbed water species [34], respectively. We use the PeakFit software to calculate the O_{ads}/$O_{lattice}$ molar ratios according to their peak area ratios. The Pt 4f$_{7/2}$ binding energy of the 0.25 Pt_1/meso-Fe_2O_3 sample was 72.9 eV (Fig. 6C), indicating that the oxidation state of the single-atom Pt was $\delta+$ ($2 < \delta < 4$) [35]. Notably, a down-shift of Pt 4f$_{7/2}$ photoemission was observed in Fig. 6F, probably due to formation of a new configuration, Pt-O(OH)$_x$. In this case, Pt was still in an oxidized state [36]. The BE of Pt° species was about 71.0 eV. XPS spectrum position of the
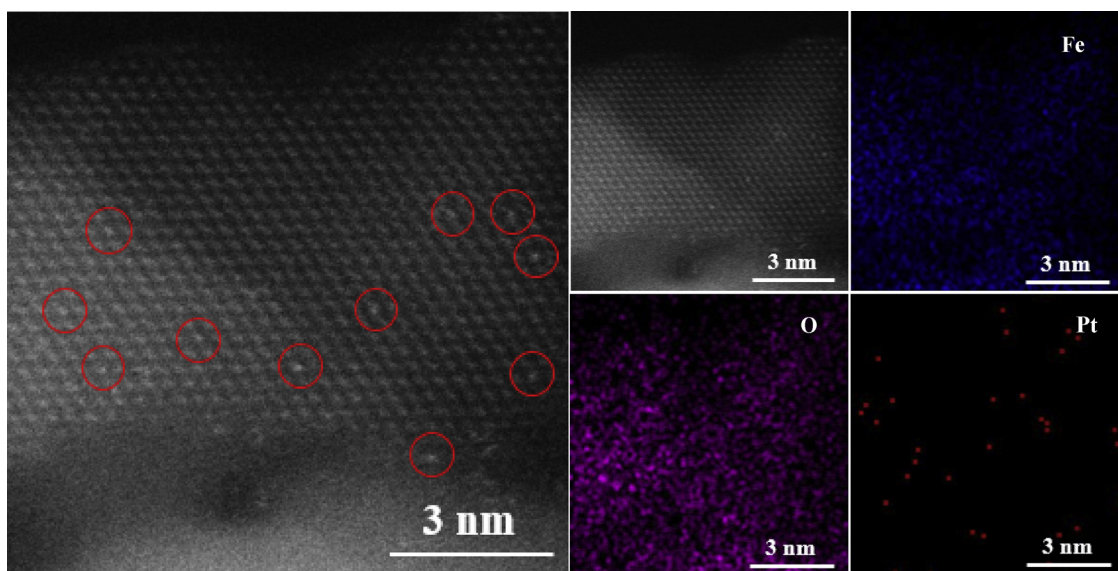
Fig. 4. Aberration-corrected HAADF-STEM image and the corresponding EDS elemental mappings of the 0.25 Pt_1/meso-Fe_2O_3 sample. Pt single atoms (white circles) are seen to be uniformly dispersed on the Fe_2O_3 support.

catalyst containing only Pt^{2+} and Pt^{4+} located at a BE of 73.0 eV [32]. There was a more amount of the Pt^{2+} species (BE = 72.9 eV) than that of the Pt^{4+} (BE = 73.6 eV) species on the surface of the 0.25 Pt_1/meso-Fe_2O_3 sample. Pt was present mainly in Pt^{4+} (BE = 73.6 eV) on the surface of the 0.25 Pt_{NP}/meso-Fe_2O_3 sample. After calcination, Pt_{NP} tended to form a high valence PtO_2, however, Pt_1 could exist stably in Pt^{2+} via the bonding of Pt-O-Fe [37]. Therefore, the BE of Pt on the surface of 0.25 Pt_1/meso-Fe_2O_3 was lower than that of Pt on the surface of 0.25 Pt_{NP}/meso-Fe_2O_3. After 50 h of benzene combustion in the presence of 3.0 vol% water, the surface of 0.25 Pt_1/meso-Fe_2O_3 generated the Pt-O(OH)$_x$ (Pt(OH)$_x$ was attached to Fe_2O_3 through oxygen ligand) species, where Pt was in atomic dispersion as Pt(II) [38]. Hence, the BE of Pt on the surface of the water-treated sample was lower than that of Pt on the surface of the fresh sample.

3.3. Reducibility

The reducibility of a material is highly related to its catalytic performance. To probe the metal-support interactions and reducibility of the samples, we conducted the H_2-TPR experiments, and their profiles are shown in Fig. 7. It is observed that there were three regions for the reduction of each sample: the peak at 80–120 °C was assignable to the

reduction of oxidized $Pt^{\delta+}$ to $Pt°$, the one at 120–370 °C was ascribable to the reduction of Fe^{3+} to Fe^{2+}, and the one at 370–700 °C was attributable to the reduction of the Fe^{2+} to Fe°. With a rise in Pt loading, the peak due to the reduction of Fe^{3+} to Fe^{2+} shifted to a lower temperature (Fig. 7). Calculation of the H_2 consumption (Table S1) indicates that in addition to the first peak at 80–120 °C, the second peak was due to the reduction of Fe^{3+} via the spillover of H atoms chemically adsorbed on the reduced Pt. The difference between the theoretical hydrogen consumption of $Pt^{\delta+}$ reduction and the H_2 consumption corresponding to the first peak was an indicator of the extent of hydrogen spillover. The higher molar ratio of Fe^{3+} reduced to Fe^{2+} (accompanying by the reduction of Pt^{2+} to Pt°) represented a more amount of Fe^{3+} reduced to Fe^{2+} by H atoms chemically adsorbed on the reduced Pt, which means H was easily moved from Pt to Fe via spillover. A more amount of hydrogen spillover represented a stronger metal-support interaction [39]. Therefore, there was a stronger interaction between Pt and meso-Fe_2O_3.

In order to evaluate the metal-support interaction quantitatively, we calculated the molar ratio of Fe^{3+} reduced to Fe^{2+} to Pt^{2+} reduced to Pt° (Table S1). Obviously, the ratio of the sing-atom Pt catalysts were higher than the Pt NP catalyst, which increased with a rise of Pt content, indicating the interaction between the single-atom Pt and the
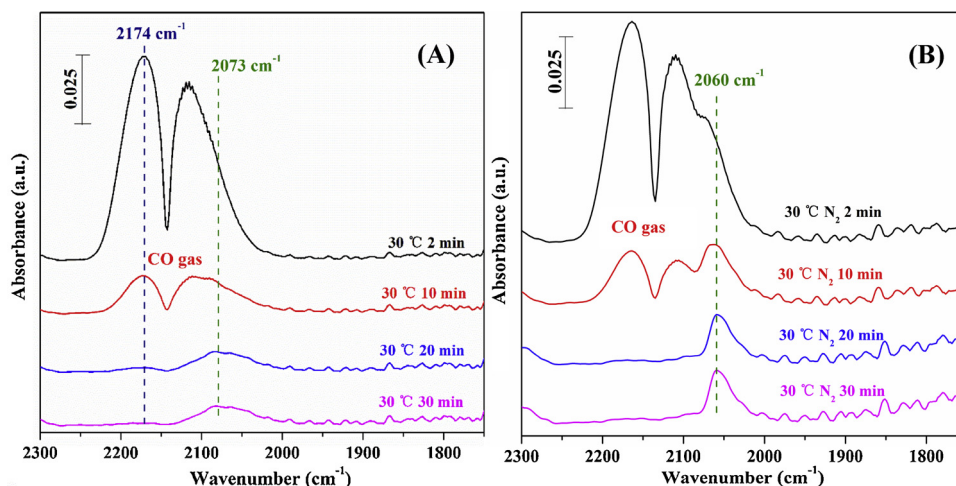

Fig. 5. In situ DRIFT spectra of CO adsorption at 30 °C for different time on (A) 0.25 Pt_1/meso-Fe_2O_3 and (B) 0.25 Pt_{NP}/meso-Fe_2O_3.
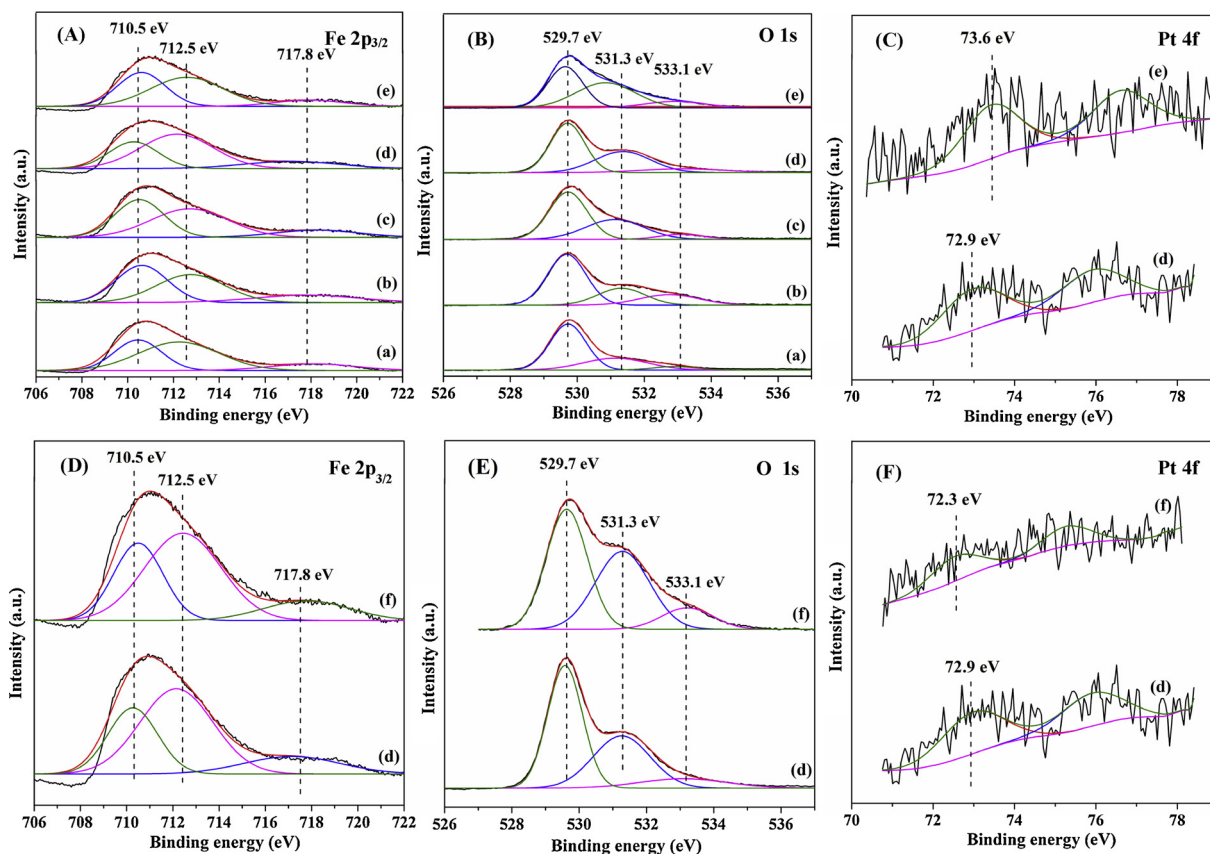
Fig. 6. (A) Fe $2p_{3/2}$, (B) O 1 s, and (C) Pt 4f XPS spectra of (a) meso-Fe$_2$O$_3$, (b) 0.08Pt$_1$/meso-Fe$_2$O$_3$, (c) 0.15Pt$_1$/meso-Fe$_2$O$_3$, (d) 0.25 Pt$_1$/meso-Fe$_2$O$_3$, and (e) 0.25 Pt$_{NP}$/meso-Fe$_2$O$_3$; and (D) Fe $2p_{3/2}$, (E) O 1 s, and (F) Pt 4f XPS spectra of the 0.25 Pt$_1$/meso-Fe$_2$O$_3$ sample (d) before and (f) after 50 h of benzene combustion in the presence of 3.0 vol% water and pretreatment in O$_2$ at 300 °C for 1 h.
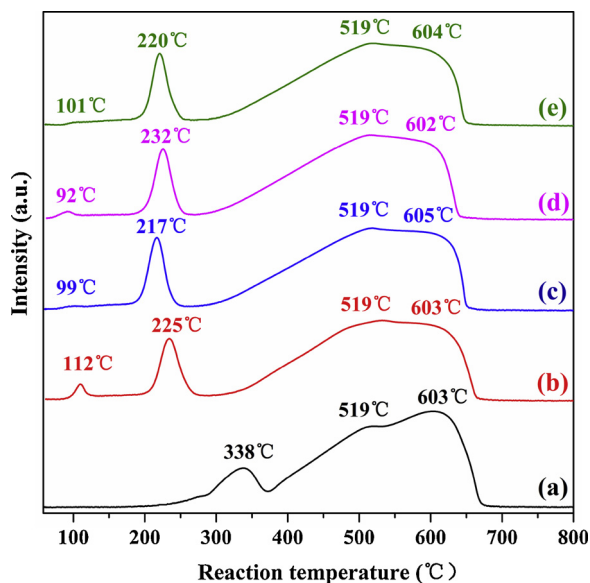

Fig. 7. H$_2$-TPR profiles of (a) meso-Fe$_2$O$_3$, (b) 0.08Pt$_1$/meso-Fe$_2$O$_3$, (c) 0.15Pt$_1$/meso-Fe$_2$O$_3$, (d) 0.25 Pt$_1$/meso-Fe$_2$O$_3$, and 0.25 Pt$_{NP}$/meso-Fe$_2$O$_3$.

meso-Fe$_2$O$_3$ support was stronger than that between the Pt NPs and the meso-Fe$_2$O$_3$ support. Such a strong interaction would be helpful for the oxidation of benzene.

3.4. Catalytic performance

Benzene, a typical VOC, was used for evaluating catalytic activities of the samples. It is obviously seen from Fig. 8A that benzene conversion increased with a rise in temperature. Unambiguously and reasonably, pure meso-Fe$_2$O$_3$ performed the worst among the samples. With the rise in Pt loading, the catalytic activity increased. The 0.25 Pt$_1$/meso-Fe$_2$O$_3$ sample showed the best catalytic activity (the temperature ($T_{90\%}$) at 90% benzene conversion = 198 °C), which was higher than that over the 1 wt% Pt–TiO$_2$–Na$_3$Ct catalyst [40]. Although the $T_{90\%}$ was higher over 0.25 Pt$_1$/meso-Fe$_2$O$_3$ than that over 1 wt% Pt–TiO$_2$–Na$_3$Ct, Pt content in our catalyst was only 1/4 of the 1 wt% Pt–TiO$_2$–Na$_3$Ct catalyst and SV was almost two times as high as that reported in the literature. Whereas the 0.25 Pt$_{NP}$/meso-Fe$_2$O$_3$ sample (the temperature ($T_{10\%}$) at 10% benzene conversion = 198 °C) was much inferior to the 0.25 Pt$_1$/meso-Fe$_2$O$_3$ sample in activity. The turnover frequency (TOF) can be calculated according to TOF = xC_0/$(nD) = x \times C_0/(m_{catalyst} \times$ actual Pt content/$M_{Pt}) \times D$, where x is the conversion at a certain temperature, C_0 (mol/s) is the initial benzene concentration per second, n (mol) is the molar amount of Pt, $m_{catalyst}$ (g) is the mass of the catalyst, M_{Pt} (g/mol) is the molar weight of Pt, and D is the metal dispersion. The benzene oxidation rates can be estimated according to the activity data and weight amounts of the catalyst. Apparently, the 0.25 Pt$_1$/meso-Fe$_2$O$_3$ sample showed much higher TOF$_{Pt}$ and reaction rate at 160 °C than 0.25 Pt$_{NP}$/meso-Fe$_2$O$_3$ (Table 2). All of the noble metal was involved in the reaction over the 0.25 Pt$_1$/meso-Fe$_2$O$_3$ sample (with Pt being dispersed in single-atom). Only the surface Pt atoms of the 0.25 Pt$_{NP}$/meso-Fe$_2$O$_3$ sample (with Pt being dispersed in NP), however, participated in the reaction. Moreover, the 0.25 Pt$_1$/meso-Fe$_2$O$_3$ sample possessed a higher Pt content than the two Pt$_1$/meso-Fe$_2$O$_3$ samples. Therefore, the 0.25 Pt$_1$/meso-Fe$_2$O$_3$ catalyst
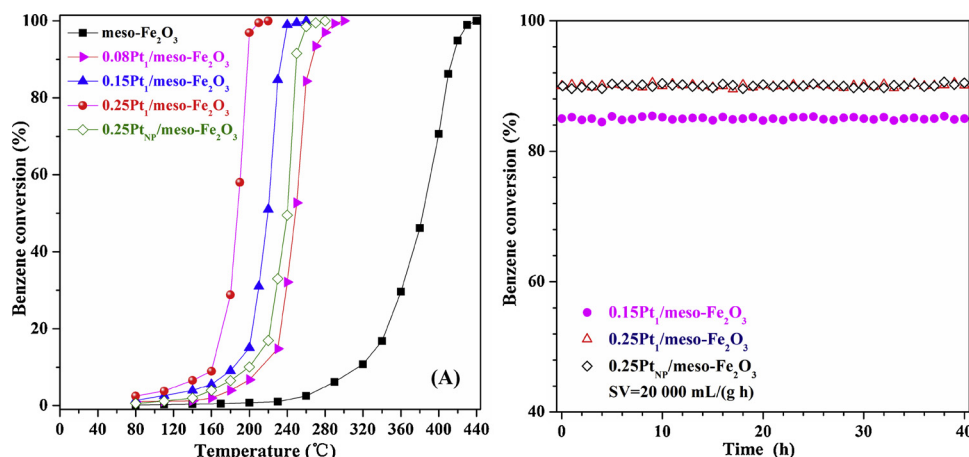
Fig. 8. Benzene conversion as a function of (A) temperature over the as-prepared samples and (B) on-stream reaction time over (●) 0.15Pt$_1$/meso-Fe$_2$O$_3$ at 230 °C, (△) 0.25 Pt$_1$/meso-Fe$_2$O$_3$ at 198 °C and (◇) 0.25 Pt$_{NP}$/meso-Fe$_2$O$_3$ at 250 °C and SV = 20,000 mL/(g h).

showed the best catalytic activity. Actually, the actual metal dispersion measured via CO chemisorption existed a certain deviation as compared with the theoretical values. In the catalytic combustion process, the active components contained not only Pt$_1$, but also Fe$_2$O$_3$ and Pt$_1$-Fe$_2$O$_3$ interface. In addition, according to the different Pt loadings, platinum density per unit area was different, giving rise to different active centers. Therefore, TOF might be associated with the reaction rate and Pt loading. Benzene and oxygen adsorption and reaction rate were different at different Pt loadings, which resulted in different TOFs. xC_0 for 0.08Pt$_1$/meso-Fe$_2$O$_3$ was much smaller than those for 0.15Pt$_1$/meso-Fe$_2$O$_3$ and 0.25 Pt$_1$/meso-Fe$_2$O$_3$, causing the TOF of the former sample to be much smaller than those of the latter two sample.

To examine the catalytic stability, we carried out on-stream benzene combustion at 230 °C over 0.15Pt$_1$/meso-Fe$_2$O$_3$, at 198 °C over 0.25 Pt$_1$/meso-Fe$_2$O$_3$, and at 250 °C over 0.25 Pt$_{NP}$/meso-Fe$_2$O$_3$. It can be seen from Fig. 8B that no significant loss in activity was observed over each of the three samples after 40 h of on-stream reaction, which was attributed to the strong interaction between Pt and meso-Fe$_2$O$_3$. Hence, the three samples were catalytically stable.

3.5. Effects of moisture and carbon dioxide on catalytic activity

It has been reported that catalytic activity for the oxidation of VOCs was negatively influenced by moisture introduced into the feed stream [41]. Therefore, it is necessary to examine the effect of H$_2$O on catalytic activity of the typical sample. We conducted benzene combustion over the 0.15Pt$_1$/meso-Fe$_2$O$_3$, 0.25 Pt$_1$/meso-Fe$_2$O$_3$, and 0.25 Pt$_{NP}$/meso-Fe$_2$O$_3$ samples in the presence of 1.0 or 3.0 vol% water vapor, and the results are shown in Fig. 9A–D. It can be realized that introduction of water vapor played a positive role in benzene combustion over the supported single-atom Pt samples. Recent studies pointed out that a small amount of water could greatly increase the activity of CO oxidation over some supported noble metal catalysts [42]. Remarkably, water might be not directly involved in these reactions. Nevertheless, moisture could play a positive role in CO oxidation over a single-atom

Pt catalyst via direct participation in the final CO$_2$ production [43]. Water participated in the reaction via the O-transfer reactions (H$_2$O → OH(W) + H, H + O → OH(L), OH(W) + CO → COOH(W), COOH(W) → H + CO$_2$(W), and H + OH(L) → H$_2$O, in which the W and L represented the O coming from water and lattice oxygen, respectively). In addition, there have been reports that the Au-(OH)$_x$ and Pt-(OH)$_x$-(Na/K)$_y$ species were active for the low-temperature water-gas shift reaction [44]. On the other hand, H$_2$O was helpful for the decomposition of carbonate [42]. The active interface sites were gradually covered with the inert carbonate species accumulated during the combustion process [45]. The deactivated catalyst could be regenerated by addition of moisture in the feed stream. Costello et al [46]. proposed a model of carbonate decomposition mechanism (CO$_3$ + H$_2$O → CO$_3$H + OH and CO$_3$H → CO$_2$ + OH). Therefore, there might be a strong promotion of water in benzene combustion via direct participation in the combustion over 0.15Pt$_1$/meso-Fe$_2$O$_3$ and 0.25 Pt$_1$/meso-Fe$_2$O$_3$. The 0.15Pt$_1$/meso-Fe$_2$O$_3$ sample with a high metal dispersion that Pt was in single-atom state possessed a high Pt-O(OH)$_x$ content, and the activity still retained at a high level after water vapor removal. For 0.25 Pt$_1$/meso-Fe$_2$O$_3$, the activity decreased after removing 3 vol% moisture, but was totally restored to the level in the absence of water vapor because of the positive effect of Pt-O(OH)$_x$ in the first cycle. In the presence of water vapor, benzene conversion maintained high levels in the second and third cycles, and after cutting off water vapor benzene conversion was higher than the initial level, which might derive from increase of the Pt-O(OH)$_x$ content. On the other hand, owing to the high Pt content, a slight amount of Pt cluster might exist in 0.25 Pt$_1$/meso-Fe$_2$O$_3$ with a relatively low metal dispersion, which was not favorable for formation of the Pt-O(OH)$_x$ species. For 0.25 Pt$_{NP}$/meso-Fe$_2$O$_3$, catalytic activity deactivation in the presence of water vapor was due to the competitive adsorption of water vapor. It should be noted that the temperature was too low to produce enough radicals, resulting in the occurrence of no significant water effect at low conversions (Fig. 9A). In contrast, water exhibited a negative effect on benzene conversion at 250 °C over 0.25 Pt$_{NP}$/meso-Fe$_2$O$_3$. The activity inhibition by water vapor was a

Table 2
Benzene oxidation activities, TOF$_{Pt}$, reaction rates at 160 °C, and metal dispersion of the samples at SV = 20,000 mL/(g h).

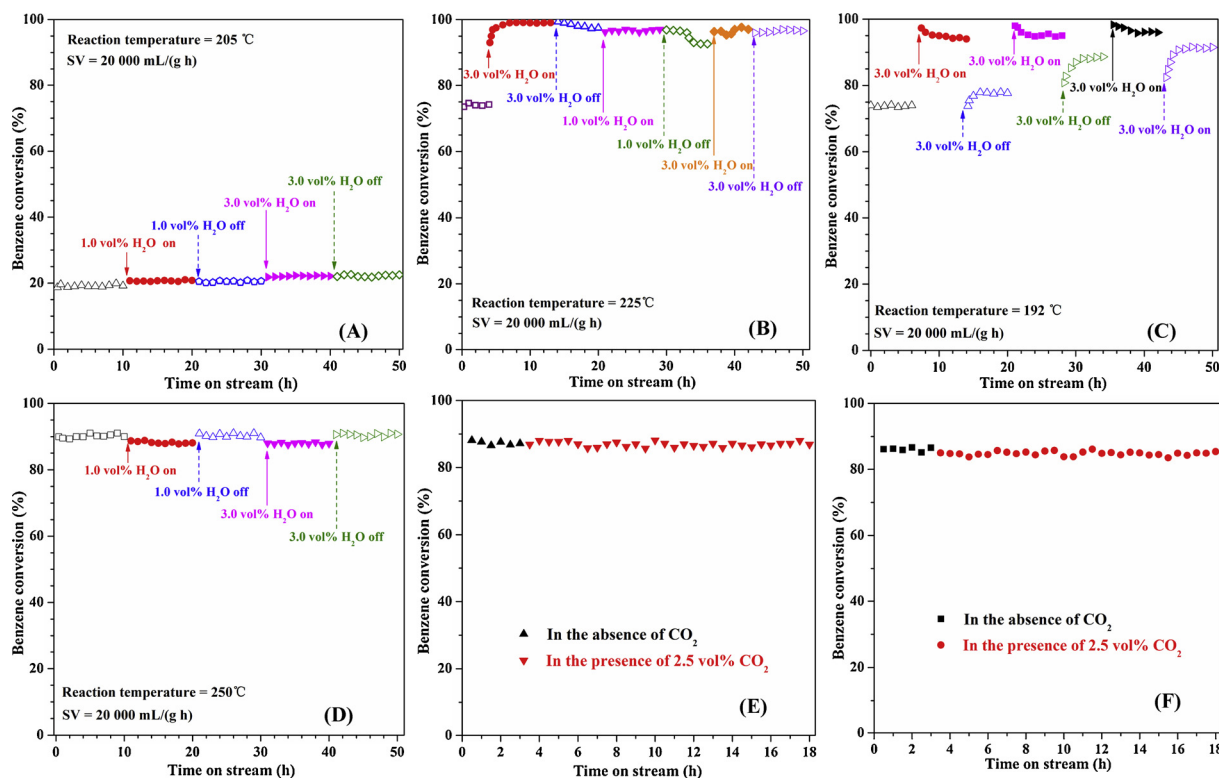| Sample	Benzene oxidation activity			Benzene oxidation at 160 °C			Metal dispersion (%)
	$T_{10\%}$ (°C)	$T_{50\%}$ (°C)	$T_{90\%}$ (°C)	Benzene conversion (%)	TOF$_{Pt}$ (s^{-1}))	Reaction rate (× 10^{-6} mol/(g s))	
meso-Fe$_2$O$_3$	320	385	415	0.45	–	1.02	–
0.08Pt$_1$/meso-Fe$_2$O$_3$	213	248	266	1.0	0.79	2.27	70.1
0.15Pt$_1$/meso-Fe$_2$O$_3$	182	219	237	5.6	2.47	12.65	66.4
0.25 Pt$_1$/meso-Fe$_2$O$_3$	164	186	198	9.7	2.69	21.99	63.5
0.25 Pt$_{NP}$/meso-Fe$_2$O$_3$	196	241	250	1.4	1.16	3.18	21.2

Fig. 9. Benzene conversion as a function of on-stream reaction time in the presence or absence of (A–D) 1.0 or 3.0 vol% water vapor and (E, F) 2.5 vol% carbon dioxide at SV = 20,000 mL/(g h) over (A) 0.15Pt$_1$/meso-Fe$_2$O$_3$ at 205 °C, (B) 0.15Pt$_1$/meso-Fe$_2$O$_3$ at 225 °C, (C, E) 0.25 Pt$_1$/meso-Fe$_2$O$_3$ at 192 °C, and (D, F) 0.25 Pt$_{NP}$/meso-Fe$_2$O$_3$ at 250 °C.

result due to the competitive adsorption of H$_2$O and benzene on the surface of 0.25 Pt$_{NP}$/meso-Fe$_2$O$_3$ [47].

Fig. 9E and F shows the effects of CO$_2$ on catalytic activity of the 0.25 Pt$_1$/meso-Fe$_2$O$_3$ and 0.25 Pt$_{NP}$/meso-Fe$_2$O$_3$ samples at SV = 20,000 mL/(g h). When 2.5 vol% CO$_2$ was added to the gas flow, benzene conversion did not change obviously over 0.25 Pt$_1$/meso-Fe$_2$O$_3$ and 0.25 Pt$_{NP}$/meso-Fe$_2$O$_3$ after 15 h of reaction, indicating that the meso-Fe$_2$O$_3$-supported Pt catalysts possessed a good carbon dioxide-resistant ability.

3.6. Possible catalytic reaction pathways

In situ DRIFTS experiments were employed to determine the possible intermediate species during the process of benzene oxidation, and the results are shown in Fig. 10. The 0.25 Pt$_1$/meso-Fe$_2$O$_3$ sample with the highest catalytic activity was used to study benzene oxidation mechanism. Fig. 10A shows desorption of benzene before the reaction. The bands at 661 and 1039 cm^{-1} were related to the C−H deformation vibrations. The band at 1483 cm^{-1} was assigned to the C═C stretching vibrations. The vibrational bands at 1966 and 1820 cm^{-1} were attributed to the C−H out-of-plane bending modes. The bands at 3088 and 3047 cm^{-1} were ascribed to the C−H stretching modes in the benzene rings [48]. The weak band at 1305 cm^{-1} was due to the ring vibrations. It is observed that, with increasing desorption time, the adsorption peaks referring to the benzene features decreased in intensity. With a rise in temperature, the intensity of benzene bands decreased gradually, and at the same time, some new IR bands appeared (Fig. 10B). In particular, the band at 1572 cm^{-1} could be assigned to the C═C stretching vibrations of the phenolate species [49], the one at 1532 cm^{-1} was attributed to the maleate species [50], and the one at
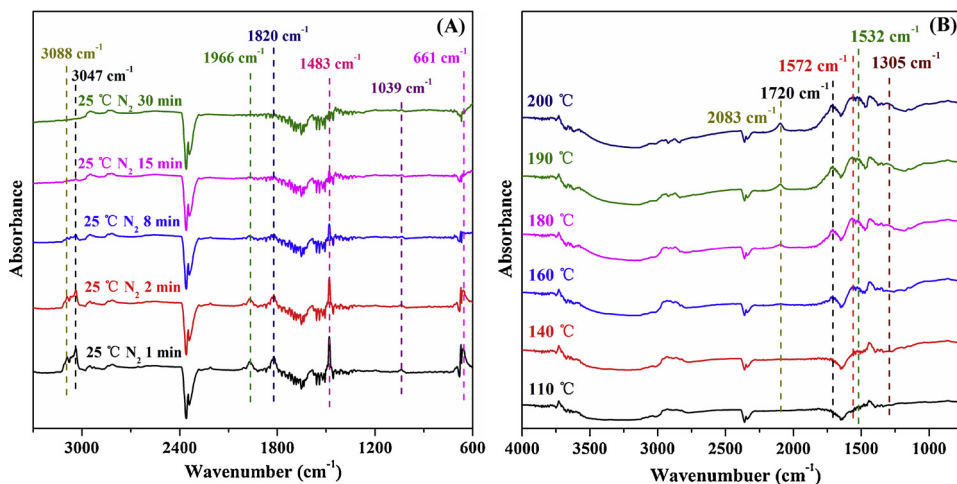

Fig. 10. (A) In situ DRIFTS spectra of benzene desorption at a temperature of 25 °C and a N$_2$ flow of 30 mL/min on the 0.25 Pt$_1$/meso-Fe$_2$O$_3$ sample that was pretreated in a gas mixture (1000 ppm benzene + 20 vol% O$_2$ + N$_2$ (balance)) flow of 16.7 mL/min at 25 °C; and (B) in situ DRIFTS spectra of benzene oxidation over the 0.25 Pt$_1$/meso-Fe$_2$O$_3$ sample under the conditions same as the catalytic activity evaluation.

$1720 \, cm^{-1}$ was tentatively ascribed to the C=O stretching vibrations of the quinone or other ketone species [51]. In addition, the band at $2083 \, cm^{-1}$ was attributed to the CO species. Combining the results of DRIFTS characterization and those reported previously [52], the oxidation of benzene might take place according to the following steps: Benzene was first oxidized into phenolates, the formed phenolates were then transformed into benzoquinone or cyclohexanone, and the aromatic rings were finally disrupted accompanying by formation of the maleate species that were further oxidized by O_2 to generate CO_2 and H_2O as the final products.

4. Discussion

Oxygen activation is a crucial step in oxidation reactions, and catalytic performance is intimately associated with the oxygen activation ability of a catalyst. It was proposed that the activation capacity of oxygen molecules was related to the oxygen vacancy density of the catalyst [53]. Among the as-prepared five samples, $0.25 \, Pt_1$/meso-Fe_2O_3 possessed the highest Fe^{2+}/Fe^{3+} and O_{ads}/O_{latt} molar ratios (Table S2), indicating the presence of the highest amount of oxygen vacancies in $0.25 \, Pt_1$/meso-Fe_2O_3. In order to confirm the relationship between the O_{ads} species amount (O_2 activation ability) and catalytic activity, we plotted the $T_{90\%}$ for benzene oxidation as a function of O_{ads}/O_{latt} molar ratio on the samples, as presented in Fig. S4. Apparently, catalytic activity was highly related to the O_{ads}/O_{latt} molar ratio, suggesting that there was an intimate relation between catalytic performance and O_{ads} species concentration. Since $0.25 \, Pt_1$/meso-Fe_2O_3 possessed the highest O_{ads}/O_{latt} molar ratio (the superior O_2 activation ability), the reaction rate over this sample was the highest. These results clearly demonstrate that catalytic performance of xPt_1/meso-Fe_2O_3 was dependent upon its oxygen activation ability.

It has been reported that the oxidation of CO over Pt_1/CeO_2 [43], formaldehyde over 3DOM Au/CeO_2-Co_3O_4 [54], and benzene over Au/ZnO [55] as well as the oxidation of hydrocarbons over transition-metal oxides (e.g., Co_3O_4 and Fe_2O_3 [56]) took place via a Mars-van Krevelen mechanism. It was also pointed out that the Fe–O bond could be weakened by Au [57], and the mobility of the lattice oxygen was increased. Lattice oxygen could participate in the reaction through a Mars–van Krevelen mechanism. Considering a weak mobility of lattice oxygen in meso-Fe_2O_3 at low temperatures, however, the xPt_1/meso-Fe_2O_3 samples would hardly follow the Mars–van Krevelen mechanism in the present conditions. In addition, an interface mechanism is usually proposed over the reducible oxide-supported Au catalysts with the oxygen species being adsorbed on surface oxygen vacancies of the support at perimeter sites [58,59], in which the oxygen species adsorbed on surface vacancies of perimeter sites were removed through the reaction with benzene adsorbed on Pt single atoms in the first step, leading to formation of H_2O and CO_2 and recovering of surface oxygen vacancies, followed by activation of gas phase oxygen at surface oxygen vacancies to the O_{ads} species. In the xPt_1/meso-Fe_2O_3 samples, due to the strong interaction between Pt_1 and meso-Fe_2O_3, surface oxygen vacancies would be generated through reduction of the Fe^{3+} to Fe^{2+} species by Pt_1, at which gas-phase oxygen molecules were activated to the active oxygen species. Furthermore, adsorption of benzene could remarkably be promoted by Pt, boosting the migration of chemisorbed benzene to the Pt_1–Fe_2O_3 interface. Consequently, benzene could be oxidized by the active oxygen species at the Pt_1–Fe_2O_3 interface. We propose that benzene oxidation might obey an interface mechanism over the xPt_1/meso-Fe_2O_3 catalysts. The detailed study on reaction mechanism needs to be carried out by in situ techniques in the future.

5. Conclusions

The meso-Fe_2O_3 and xPt_1/meso-Fe_2O_3 samples were prepared using the KIT-6-templating and PVA-protected reduction methods, respectively. The $0.15Pt_1$/meso-Fe_2O_3 and $0.25 \, Pt_1$/meso-Fe_2O_3 samples exhibited higher catalytic activities than the $0.25 \, Pt_{NP}$/meso-Fe_2O_3 sample for benzene combustion, and $0.25 \, Pt_1$/meso-Fe_2O_3 performed the best, giving rise to a benzene conversion of 90% at 198 °C and a reaction rate seven times higher than that over $0.25 \, Pt_{NP}$/meso-Fe_2O_3. The good catalytic performance of $0.25 \, Pt_1$/meso-Fe_2O_3 was associated with the high utilization of Pt atoms. Furthermore, the $0.15Pt_1$/meso-Fe_2O_3 and $0.25 \, Pt_1$/meso-Fe_2O_3 samples were water-resistant, which was attributed to formation of the active radicals and decomposition of carbonates. In situ DRIFTS results demonstrate formation of the phenolate and benzoquinone as well as cyclohexanone and maleate, which were the main intermediates in the oxidation of benzene. The good stability of the $0.15Pt_1$/meso-Fe_2O_3 and $0.25 \, Pt_1$/meso-Fe_2O_3 samples was associated with the strong interaction between Pt and meso-Fe_2O_3. In addition, the $0.25 \, Pt_1$/meso-Fe_2O_3 sample possessed a good carbon dioxide-resistant ability. We believe that this work is meaningful in designing single-atom catalysts for the oxidative removal of VOCs.

Appendix A. Supplementary data

Supplementary material related to this article can be found, in the online version, at doi:https://doi.org/10.1016/j.apcatb.2018.11.077.

References

[1] A.L. Bolden, C.F. Kwiatkowski, T. Colborn, New look at BTEX: are ambient levels a problem? Environ. Sci. Technol. 49 (2015) 5261–5276.
[2] S.C. Kim, W.G. Shim, Catalytic combustion of VOCs over a series of manganese oxide catalysts, Appl. Catal. B 98 (2010) 180–185.
[3] H.X. Dai, Environmental catalysis: a solution for the removal of atmospheric pollutants, Sci. Bull. 60 (2015) 1708–1710.
[4] S. Zhao, F.Y. Hu, J.H. Li, Hierarchical core-shell Al$_2$O$_3$@Pd-CoAlO microspheres for low-temperature toluene combustion, ACS Catal. 6 (2016) 3433–3441.
[5] T.D. Pham, B.K. Lee, C.H. Lee, The advanced removal of benzene from aerosols by photocatalytic oxidation and adsorption of Cu–TiO$_2$/PU under visible light irradiation, Appl. Catal. B 182 (2016) 172–183.
[6] X.F. Qian, M. Ren, D.T. Yue, Y. Zhu, Y. Han, Z.F. Bian, Y.X. Zhao, Mesoporous TiO$_2$ films coated on carbon foam based on waste polyurethane for enhanced photocatalytic oxidation of VOCs, Appl. Catal. B 212 (2017) 1–6.
[7] X.F. Yang, A.Q. Wang, B.T. Qiao, J. Li, J.Y. Liu, Single-atom catalysts: a new frontier in heterogeneous catalysis, Acc. Chem. Res. 46 (2013) 1740–1748.
[8] Z. Ma, S. Dai, Design of novel structured gold nanocatalysts, ACS Catal. 1 (2011) 805–818.
[9] Y.X. Zhao, Z.Y. Li, Z. Yuan, X.N. Li, S.G. He, Thermal methane conversion to formaldehyde promoted by single platinum atoms in PtAl$_2$O$_4$$^-$ cluster anions, Angew. Chem. Int. Ed. 126 (2014) 9636–9640.
[10] B.T. Qiao, A.Q. Wang, X.F. Yang, L.F. Allard, Z. Jiang, Y.T. Cui, J.Y. Liu, J. Li, T. Zhang, Single-atom catalysis of CO oxidation using Pt$_1$/FeO$_x$, Nat. Chem. 3 (2011) 634–641.
[11] G. Kyriakou, M.B. Boucher, A.D. Jewell, E.A. Lewis, T.J. Lawton, A.E. Baber, H.L. Tierney, M. Flytzani-Stephanopoulos, E.C.H. Sykes, Isolated metal atom geometries as a strategy for selective heterogeneous hydrogenations, Science 335 (2012) 1209–1212.
[12] J.J. Shan, J.L. Liu, M.W. Li, S. Lustig, S. Lee, M. Flytzani-Stephanopoulos, NiCu single atom alloys catalyze the CeH bond activation in the selective non- oxidative ethanol dehydrogenation reaction, Appl. Catal. B 226 (2018) 534–543.
[13] X.N. Li, Z. Yuan, S.G. He, CO oxidation promoted by gold atoms supported on titanium oxide cluster anions, J. Am. Chem. Soc. 136 (2014) 3617–3623.
[14] H. Yan, H. Cheng, H. Yi, Y. Lin, T. Yao, C. Wang, J. Li, S. Wei, J. Lu, Single-atom Pd$_1$/graphene catalyst achieved by atomic layer deposition: remarkable performance in selective hydrogenation of 1,3-butadiene, J. Am. Chem. Soc. 137 (2015) 10484–10487.
[15] M. Moses-DeBusk, M. Yoon, L.F. Allard, D.R. Mullins, Z.L. Wu, X.F. Yang, G. Veith, G.M. Stocks, C.K. Narula, CO oxidation on supported single Pt atoms: experimental and ab initio density functional studies of CO interaction with Pt atom on θ-Al$_2$O$_3$(010) surface, J. Am. Chem. Soc. 135 (2013) 12634–12645.
[16] X.K. Gu, B.T. Qiao, Supported single Pt$_1$/Au$_1$ atoms for methanol steam reforming, ACS Catal. 4 (2014) 3886–3890.
[17] J.Y. Liu, Catalysis by supported single metal atoms, ACS Catal. 7 (2017) 34–59.
[18] Y.J. Chen, S.F. Ji, Y.G. Wang, J.C. Dong, W.X. Chen, Z. Li, R.G. Shen, L.R. Zheng, Z.B. Zhuang, D.S. Wang, Y.D. Li, Isolated single iron atoms anchored on N-doped

porous carbon as an efficient electrocatalyst for the oxygen reduction reaction, Angew. Chem. Int. Ed. 56 (2017) 6937–6941.

[19] K. Fujiwara, S.E. Pratsinis, Single Pd atoms on TiO_2 dominate photocatalytic NO_x removal, Appl. Catal. B 226 (2018) 127–134.

[20] R. Trofimovaite, C.M.A. Parlett, S. Kumar, L. Frattini, M.A. Isaacs, K. Wilson, L. Olivi, B. Goulson, J. Debgupta, R.E. Douthwaite, A.F. Lee, Single atom Cu(I) promoted mesoporous titanias for photocatalytic methyl orange depollution and H_2 production, Appl. Catal. B 232 (2018) 501–511.

[21] W.G. Liu, L.L. Zhang, W.S. Yan, X.Y. Liu, X.F. Yang, S. Miao, W.T. Wang, A.Q. Wang, T. Zhang, Single-atom dispersed Co-N-C catalyst: structure identification and performance for hydrogenative coupling of nitroarenes, Chem. Sci. 7 (2016) 5758–5764.

[22] S.H. Xie, Y.X. Liu, J.G. Deng, J. Yang, X.T. Zhao, Z. Han, K.F. Zhang, H.X. Dai, Insights into the active sites of ordered mesoporous cobalt oxide catalysts for the total oxidation of benzene, J. Catal. 352 (2017) 282–292.

[23] Z.X. Wu, J.G. Deng, S.H. Xie, H.G. Yang, K.F. Zhang, H.X. Lin, H.X. Dai, G.S. Guo, Mesoporous Cr_2O_3supported Au-Pd alloy nanoparticles: high-performance catalysts for the oxidation of toluene, Microporous Mesoporous Mater. 224 (2016) 311–322.

[24] P. Xu, Z.X. Wu, J.G. Deng, Y.X. Liu, S.H. Xie, G.S. Guo, H.X. Dai, Catalytic performance enhancement by alloying Pd with Pt on ordered mesoporous manganese oxide for methane combustion, Chin. J. Catal. 38 (2017) 92–105.

[25] F. Kleitz, S.H. Choi, R. Ryoo, Cubic *Ia3d*large mesoporous silica: Synthesis and replication to platinum nanowires, carbon nanorods and carbon nanotubes, Chem. Commun. 9 (2003) 2136–2137.

[26] F. Kapteijn, J.A. Moulijn, A. Tarfaoui, Catalyst characterization and mimicking pretreatment procedures by temperature-programmed techniques, Stud. Surf. Sci. Catal. 123 (1999) 525–541.

[27] C. Asokan, L. DeRita, P. Christopher, Using probe molecule FTIR spectroscopy to identify and characterize Pt-group metal based single atom catalysts, Chin. J. Catal. 38 (2017) 1473–1480.

[28] K. Chakarova, M. Mihaylov, K. Hadjiivanov, FTIR spectroscopic study of CO adsorption on Pt-H-ZSM-5, Microporous Mesoporous Mater. 81 (2005) 305–312.

[29] K.L. Ding, A. Gulec, A.M. Johnson, N.M. Schweitzer, G.D. Stucky, L.D. Marks, P.C. Stair, Identification of active sites in CO oxidation and water-gas shift over supported Pt catalysts, Science 350 (2015) 189–192.

[30] H. Borchert, D. Fenske, J.K. Olesiak, J. Parisi, K.A. Shamery, M. Bäumer, Ligand-capped Pt nanocrystals as oxide-supported catalysts: FTIR spectroscopic investigations of the adsorption and oxidation of CO, Angew. Chem. Int. Ed. 46 (2007) 2923–2926.

[31] Z.L. Zhang, Y.H. Zhu, H. Asakura, B. Zhang, J.G. Zhang, M.X. Zhou, Y. Han, T. Tanaka, A.Q. Wang, T. Zhang, N. Yan, Thermally stable single atom Pt/*m*-Al_2O_3 for selective hydrogenation and CO oxidation, Nat. Commun. 8 (2017) 16100–16109.

[32] V.L. Zholobenko, G.D. Lei, B.T. Carvill, B.A. Lerner, W.M.H. Sachtler, Identification of isolated Pt atoms in H-mordenite, J. Chem. Soc. Faraday Trans. 90 (1994) 233–238.

[33] T. Yamashita, P. Hayes, Analysis of XPS spectra of Fe^{2+} and Fe^{3+} ions in oxide materials, Appl. Surf. Sci. 254 (2008) 2441–2449.

[34] S.H. Xie, J.G. Deng, S.M. Zang, H.G. Yang, G.S. Guo, H. Arandiyan, H.X. Dai, Au–Pd/3DOM Co_3O_4: highly active and stable nanocatalysts for toluene oxidation, J. Catal. 322 (2015) 38–48.

[35] B. Parthasarathi, G. Arup, M.S. Hegde, N.P. Lalla, S. Lorenzo, F. Francesco, A. Francesco, Promoting effect of CeO_2 in combustion synthesized Pt/CeO_2 catalyst for CO oxidation, J. Phys. Chem. B 107 (2003) 6122–6130.

[36] L. Wang, S.R. Zhang, Y. Zhu, A. Patlolla, J.J. Shan, H. Yoshida, S. Takeda, A.I. Frenkel, F. Tao, Catalysis and in situ studies of Rh_1/Co_3O_4 nanorods in reduction of NO with H_2, ACS Catal. 3 (2013) 1011–1019.

[37] H.F. Xiong, S. Lin, J. Goetze, P. Pletcher, H. Guo, L. Kovarik, K. Artyushkova, B.M. Weckhuysen, A.K. Datye, Thermally stable and regenerable platinum–tin clusters for propane dehydrogenation prepared by atom trapping on ceria, Angew. Chem. Int. Ed. 56 (2017) 1–7.

[38] M. Yang, J.L. Liu, S. Lee, B. Zugic, J. Huang, L.F. Allard, M. Flytzani-Stephanopoulos, A common single-site Pt(II)-O(OH)$_x$-species stabilized by sodium on "active" and "inert" supports catalyzes the water-gas shift reaction, J. Am. Chem. Soc. 137 (2015) 3470–3473.

[39] H.S. Wei, X.Y. Liu, A.Q. Wang, L.L. Zhang, B.T. Qiao, X.F. Yang, Y.Q. Huang, S. Miao, J.Y. Liu, T. Zhang, FeO_x-supported platinum single-atom and pseudo-single-atom catalysts for chemoselective hydrogenation of functionalized nitroarenes, Nat. Commun. 5 (2014) 5634–5641.

[40] Z.H. Li, K. Yang, G. Liu, G.F. Deng, J.Q. Li, G. Li, R.L. Yue, J. Yang, Y.F. Chen, Effect of reduction treatment on structural properties of TiO_2 supported Pt nanoparticles and their catalytic activity for benzene oxidation, Catal. Lett. 144 (2014) 1080–1087.

[41] S.H. Xie, H.X. Dai, J.G. Deng, Y.X. Liu, H.G. Yang, Y. Jiang, W. Tan, A.S. Ao, G.S. Guo, Au/3DOM Co_3O_4: highly active nanocatalysts for the oxidation of carbon monoxide and toluene, Nanoscale 5 (2013) 11207–11219.

[42] M. Daté, M. Okumura, S. Tsubota, M. Haruta, Vital role of moisture in the catalytic activity of supported gold nanoparticles, Angew. Chem. Int. Ed. 43 (2004) 2129–2132.

[43] C.L. Wang, X.K. Gu, H. Yan, Y. Lin, J.J. Li, D.D. Liu, W.X. Li, J.L. Lu, Water-mediated Mars-van Krevelen mechanism for CO oxidation on ceria supported single-atom Pt catalyst, ACS Catal. 1 (2017) 887–891.

[44] M. Yang, S. Li, Y. Wang, J.A. Herron, Y. Xu, L.F. Allard, S. Lee, J. Huang, M. Mavrikakis, M. Flytzani-Stephanopoulos, Catalytically active Au-O(OH)$_x$-species stabilized by alkali ions on zeolites and mesoporous oxides, Science 346 (2014) 1498–1051.

[45] F. Boccuzzi, S. Tsubota, M. Harutab, Vibrational investigation of CO adsorbed on gold deposited on TiO_2, J. Electron Spectrosc. Relat. Phenom. 64/65 (1993) 241–250.

[46] C.K. Costello, J.H. Yang, H.Y. Law, Y. Wang, J.N. Lin, L.D. Marks, M.C. Kung, H.H. Kung, On the potential role of hydroxyl groups in CO oxidation over Au/Al_2O_3, Appl. Catal. A Gen. 243 (2003) 15–24.

[47] S.H. Xie, H.X. Dai, J.G. Deng, H.G. Yang, W. Han, H. Arandiyan, G.S. Guo, Preparation and high catalytic performance of Au/3DOM Mn_2O_3 for the oxidation of carbon monoxide and toluene, J. Hazard. Mater. 279 (2014) 392–401.

[48] N. Sivasankar, S. Vasudevan, Temperature-programmed desorption and infrared spectroscopic studies of benzene adsorption in zeolite ZSM-5, J. Phys. Chem. B 108 (2004) 11585–11590.

[49] J. Bandara, J.A. Mielczarski, J.I. Kiwi, Adsorption mechanism of chlorophenols on iron oxides, titanium oxide and aluminum oxide as detected by infrared spectroscopy, Appl. Catal. B 34 (2001) 307–320.

[50] J. Lichtenberger, M.D. Amiridis, Catalytic oxidation of chlorinated benzenes over V_2O_5/TiO_2 catalysts, J. Catal. 223 (2004) 96–308.

[51] X.L. Liu, J.L. Zeng, W.B. Shi, J. Wang, T.Y. Zhu, Y.F. Chen, Catalytic oxidation of benzene over ruthenium–cobalt bimetallic catalysts and study of its mechanism, Catal. Sci. Technol. 7 (2017) 213–221.

[52] X.L. Weng, P.F. Sun, Y. Long, Q.J. Meng, Z.B. Wu, Catalytic oxidation of chlorobenzene over $Mn_xCe_{1-x}O_2$/HZSM-5 catalysts: a study with practical implications, Environ. Sci. Technol. 51 (2017) 8057–8066.

[53] Y.X. Liu, H.X. Dai, J.G. Deng, X.W. Li, Wang Y, H. Arandiyan, S.H. Xie, H.G. Yang, H.S. Guo, Au/3DOM $La_{0.6}Sr_{0.4}MnO_3$: highly active nanocatalysts for oxidation of carbon monoxide and toluene, J. Catal. 305 (2013) 146–153.

[54] B.C. Liu, Y. Liu, C.Y. Li, W.T. Hua, P. Jing, Q. Wang, J. Zhang, Three-dimensionally ordered macroporous Au/CeO_2-Co_3O_4 catalysts with nanoporous walls for enhanced catalytic oxidation of formaldehyde, Appl. Catal. B 127 (2012) 47–58.

[55] H.J. Wu, L.D. Wang, J.Q. Zhang, Z.Y. Shen, J.H. Zhao, Catalytic oxidation of benzene, toluene and *p*-xylene over colloidal gold supported on zinc oxide catalyst, Catal. Commun. 12 (2011) 859–865.

[56] S. Scirè, L.F. Liotta, Supported gold catalysts for the total oxidation of volatile organic compounds, Appl. Catal. B 125 (2012) 222–246.

[57] S. Minicò, S. Scirè, C. Crisafulli, R. Maggiore, S. Galvagno, Catalytic combustion of volatile organic compounds on gold/iron oxide catalysts, Appl. Catal. B 28 (2000) 245–251.

[58] N. Lopez, T.V.W. Janssens, B.S. Clausen, Y. Xu, M. Mavrikakis, T. Bligaard, J.K. Nørskov, On the origin of the catalytic activity of gold nanoparticles for low-temperature CO oxidation, J. Catal. 223 (2004) 232–235.

[59] H.C. Liu, A.I. Kozlov, A.P. Kozlova, T. Shido, K. Asakura, Y. Iwasawa, Active oxygen species and mechanism for low-temperature CO oxidation reaction on a TiO_2-supported Au catalyst prepared from Au(PPh$_3$)(NO$_3$) and as-precipitated titanium hydroxide, J. Catal. 185 (1999) 252–264.